ACS APPLIED NANO MATERIALS

www.acsanm.org

Article

Manipulation of Energy Migration in Upconversion Nanoparticles for Long-Lived Mn^{2+} Emission and Enhanced Singlet Molecular Oxygen Generation

Zahid U. Khan,* Latif U. Khan, Fernanda M. Prado, Iram Gul, Thiago Lopes, Leonardo M. A. Ribeiro, Mauro Bertotti, Magnus Gidlund, Hermi F. Brito,* and Paolo Di Mascio*

Cite This: *ACS Appl. Nano Mater.* 2024, 7, 21104−21113

Read Online

ACCESS | Metrics & More | Article Recommendations | Supporting Information

ABSTRACT: Nanosensitizers having long-lived upconversion emission under near-infrared (NIR) excitation offer unique advantages in terms of reduced background noise and prolonged signal detection for deep tissue therapy of cancer. Herein, we demonstrate a systematic mechanism of energy migration toward achieving long-lived Mn^{2+} upconversion emission in the multilayered core−shell−shell lattice of $NaGdF_4$:Yb^{3+},Tm^{3+},Ca^{2+}/$NaGdF_4$:Yb^{3+},Ca^{2+}/$NaGdF_4$:Mn^{2+} upconversion nanoparticles (NPs), following the Yb^{3+} → Tm^{3+} → Gd^{3+} → Mn^{2+} intermetal ions energy transfer pathway. Furthermore, a rational design of nanosensitizer was achieved by incorporating Er^{3+} ions into the intermediate shell of multishell NPs, which was subsequently conjugated with the Rose Bengal sensitizer to enable the enhancement in singlet molecular oxygen ($^1O_2$) generation under excitation of a 980 nm NIR laser. An intense higher-energy emission in the UV−blue visible region from Tm^{3+} was achieved by optimizing the amount of Ca^{2+} in the core−shell NPs, followed by subsequent energy migration to the Mn^{2+} ion incorporated at the outer shell. The Mn^{2+} ions were strategically doped in the outer shell of NPs to leverage the catalytic activities of Mn^{2+} for H_2O_2 decomposition and decrease the backward energy transfer to the Tm^{3+} ion. Hence, this approach resulted in a long lifetime of Mn^{2+} (∼34 ms), attributed to the spin-forbidden $^4T_{1g}$ → $^6A_{1g}$ transition within $3d^5$ configuration. Additionally, the nanosensitizer demonstrated high $^1O_2$ (∼0.39 μM) generation even at a very low concentration (5 μg/mL) under a laser power of 2 mW cm^{-2}. The hydrogenase-like catalytic activities of Mn^{2+} exhibited significant oxygen production through decomposition of H_2O_2. Hence, these findings might contribute to the development of convenient multifunctional nanosensitizers for multimodal bioimaging and therapeutic features, including efficient $^1O_2$ generation and catalytic decomposition of H_2O_2 (found excessively in a tumor environment) to oxygen for alleviating the hypoxia.

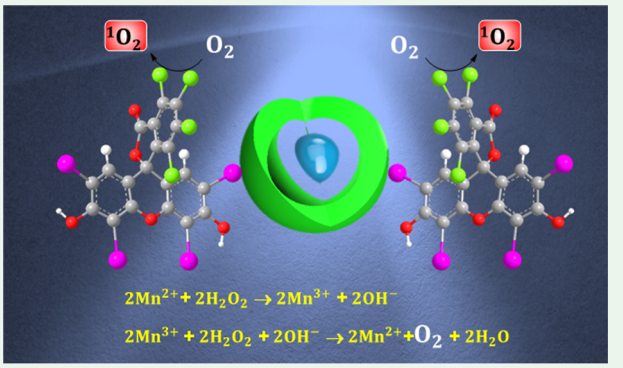

KEYWORDS: *upconversion nanoparticles, nanosensitizer, singlet molecular oxygen generation, lanthanides, manganese, hypoxia*

1. INTRODUCTION

Singlet molecular oxygen ($^1O_2$) has sparked a great deal of interest in the scientific community owing to a wide range of applications, including cancer therapeutics, smart drug delivery, biomaterials modification, and antiparasitic and antimicrobial therapy.[1−7] Since the direct excitation of oxygen from the triplet ground state to the singlet excited state is spin-forbidden ($^3O_2$ → $^1O_2$), various extended conjugated π-electronic systems containing organic or metalorganic photosensitizers are used to produce $^1O_2$.[1−3] However, they are usually excited by UV−visible light,[2,6] and the effective penetration of UV−visible light to deep tissues and solid tumors is significantly hindered due to the insufficient transmission and high scattering and absorption of light by biomolecules, thus impeding the lethality of photodynamic therapy (PDT).[1,5,6,8,9] For this purpose, lanthanide (Ln^{3+})-doped upconversion nanomaterials hold great promise due to their unique photoluminescence (PL) properties, i.e., plentiful energy states, background-free detection owing to a large anti-Stokes shifts, dopant-dependent multicolor emission, excellent photostability without bleaching and blinking, a multitude of sharp emissions in the UV−visible and near-infrared (NIR) regions, and long luminescence lifetimes.[5,6,8−17] Thus, photon upconversion in lanthanide-doped nanomaterials by combining two or more than two lower-energy optical photons into single

Received: July 26, 2024
Revised: August 22, 2024
Accepted: August 27, 2024
Published: September 3, 2024

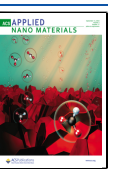

Scheme 1. Rational Design and Fabrication of $NaGdF_4:Yb^{3+},Tm^{3+},Ca^{2+}/NaGdF_4:Yb^{3+},Ca^{2+}/NaGdF_4:Mn^{2+}$ Multilayered Core−Shell−Shell NPs, including Ligand Replacement of OA by BF_4^- Followed by PEI, and the Development of the Nanosensitizer for Efficient $^1O_2$ Generation (a); Schematic Illustration (Left) and Proposed Energy Transfer Mechanism (Right) toward Long-Lived Mn^{2+} Upconversion Emission in the Core−Shell−Shell Lattice of NPs Involving the $Yb^{3+} \rightarrow Tm^{3+} \rightarrow Gd^{3+} \rightarrow Mn^{2+}$ Pathway (b)[a]

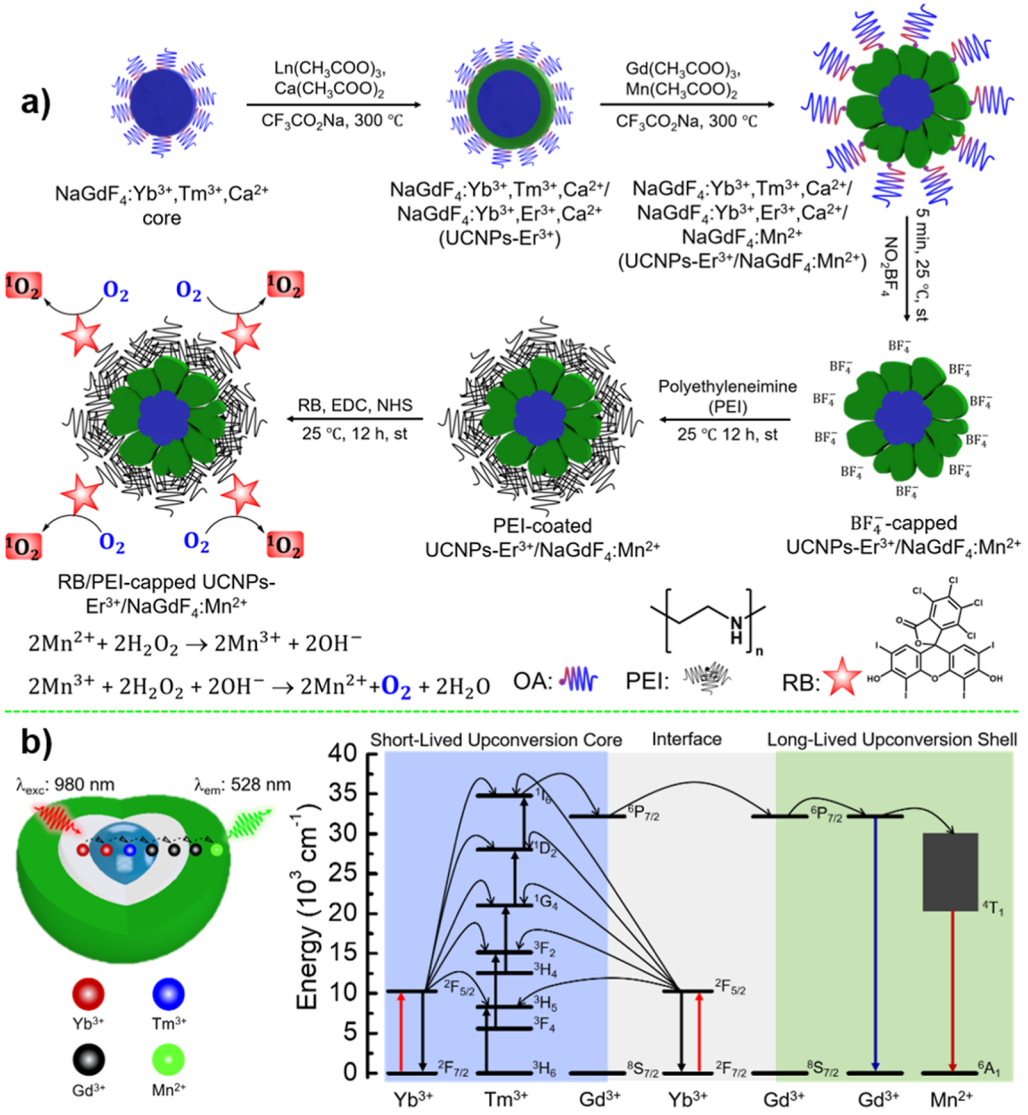

[a]The energy transfer mechanism reveals that upon irradiation at around 980 nm, Yb^{3+} ions are excited from the ground state to an excited state. The excited Yb^{3+} ions then transfer energy to Tm^{3+} ions, followed by transferring it to the Gd^{3+} mediator. Finally, the energy is transferred from Gd^{3+} to Mn^{2+} ions strategically doped in the outer shell. The multilayered core−shell−shell regions are highlighted with blue−gray−green colors, respectively. Abbreviations: RB (Rose Bengal); EDC (1-ethyl-3-(3-dimethylaminopropyl) carbodiimide); and NHS (*N*-hydroxy succinimide).

higher-energy photon offers superior advantages owning to the remarkable features of deep tissue penetration through the NIR optical transparent biological window and negligible autofluorescence background.[6−8]

Furthermore, upconversion luminescence provides a more efficient approach to mitigating the photo damages inflicted on the biological tissues when compared to downconversion luminescence.[5,7] Among the trivalent lanthanide ions, Ho^{3+}, Er^{3+}, and Tm^{3+} have been widely studied as excellent activators along with Yb^{3+} and Nd^{3+} ions as sensitizers for the upconversion process.[5−9,11,13−16] Moreover, lanthanide-based upconversion materials exhibit ladder-like energy levels, displaying multiple emissions ranging from UV−visible to NIR regions.[6,15] These emissions can be strategically aligned with the excitation state of the molecular acceptor, thus potentially transferring the energy from NPs to the molecular sensitizer.[9]

Nanosensitizers having long-lived emissions offer multiple benefits in biomedical applications. For instance, they allow one to collect the signal/data over a longer time frame, thus improving the signal-to-noise ratio and preventing autofluorescence. They enable highly precise monitoring of the cellular process, assessing metabolic activities, and tracking of drug and biodistribution within the body.[10,18] Recent studies suggest that Mn^{2+} ions exhibit longer lifetime upconversion emission than the Ln^{3+} ions owing to the spin-forbidden optical transition within $3d^5$ configuration.[15,16] Therefore, the incorporation of Mn^{2+} ions into NPs is particularly appealing

https://doi.org/10.1021/acsanm.4c04307
ACS Appl. Nano Mater. 2024, 7, 21104−21113

Table 1. Samples Reference Table: Names and Labels

sample names	labels
$NaGdF_4:Yb^{3+},Tm^{3+},Ca^{2+}/NaGdF_4:Yb^{3+},Ca^{2+}$	UCNPs
$NaGdF_4:Yb^{3+},Tm^{3+},Ca^{2+}/NaGdF_4:Yb^{3+},Ca^{2+}/NaGdF_4:xCa^{2+},Mn^{2+}$ (x: 0, 12, 24, 36, 48, 60, and 70 mol %)	$UCNPs/NaGdF_4:xCa^{2+},Mn^{2+}$
$NaGdF_4:Yb^{3+},Tm^{3+},Ca^{2+}/NaGdF_4:Yb^{3+},Ca^{2+}/NaGdF_4:Mn^{2+}$	$UCNPs/NaGdF_4:Mn^{2+}$
$NaGdF_4:Yb^{3+},Tm^{3+},Ca^{2+}/NaGdF_4:Yb^{3+},Ca^{2+}/CaF_2:Mn^{2+}$	$UCNPs/CaF_2:Mn^{2+}$
$NaGdF_4:Yb^{3+},Tm^{3+},Ca^{2+}/NaGdF_4:Yb^{3+},Er^{3+},Ca^{2+}$	$UCNPs:Er^{3+}$
$NaGdF_4:Yb^{3+},Tm^{3+},Ca^{2+}/NaGdF_4:Yb^{3+},Er^{3+},Ca^{2+}/NaGdF_4$	$UCNPs:Er^{3+}/NaGdF_4$
$NaGdF_4:Yb^{3+},Tm^{3+},Ca^{2+}/NaGdF_4:Yb^{3+},Er^{3+},Ca^{2+}/NaGdF_4:Mn^{2+}$	$UCNPs:Er^{3+}/NaGdF_4:Mn^{2+}$
$NaGdF_4:Yb^{3+},Tm^{3+},Ca^{2+}/NaGdF_4:Yb^{3+},Er^{3+},Ca^{2+}/CaF_2:Mn^{2+}$	$UCNPs:Er^{3+}/CaF_2:Mn^{2+}$

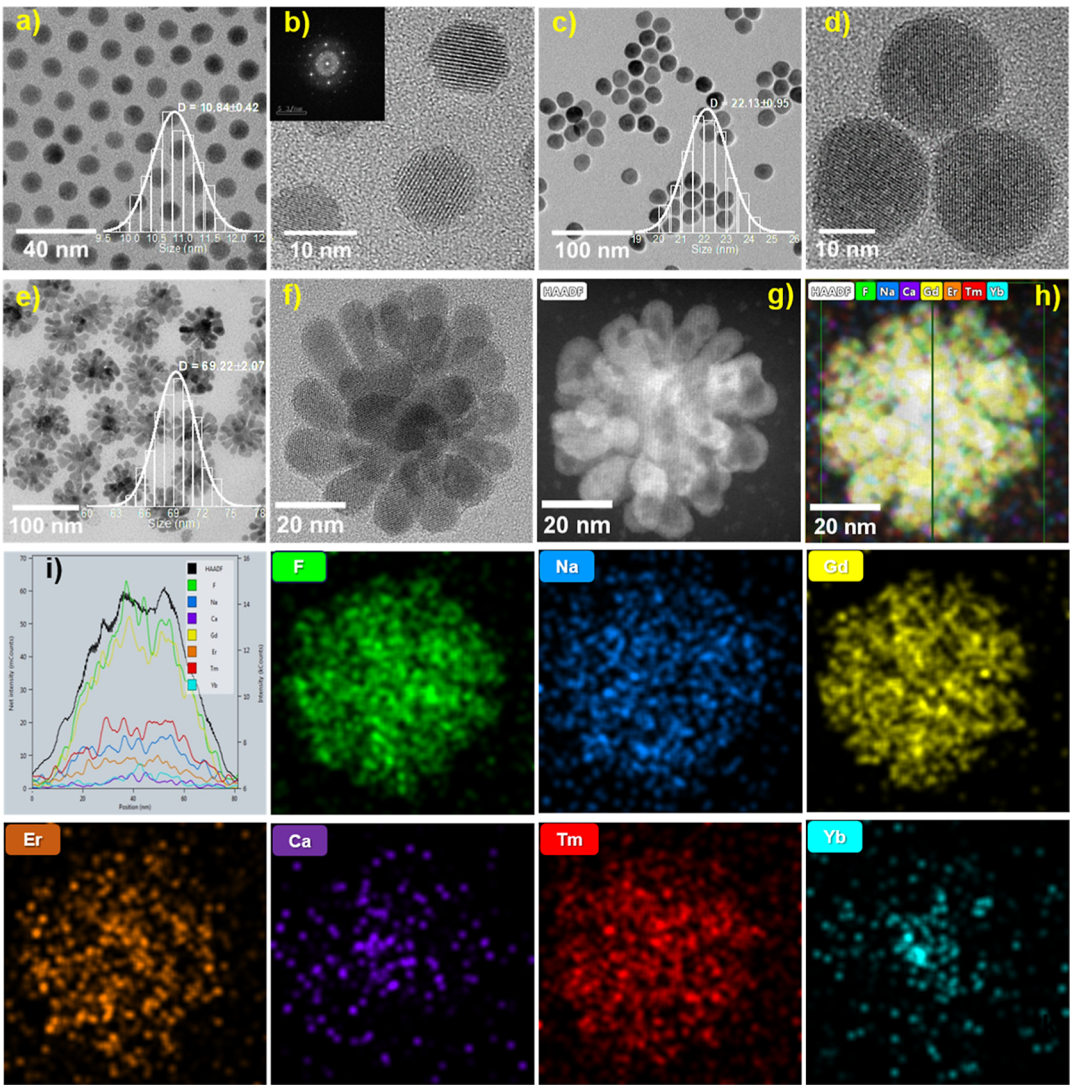

Figure 1. High-resolution TEM images and the corresponding size distribution histogram of UCNPs: $NaGdF_4:Yb^{3+},Tm^{3+},Ca^{2+}$ core (a,b), UCNPs:Er^{3+} core−shell NPs (c,d), and UCNPs:$Er^{3+}/NaGdF_4$ core−shell−shell NPs (e−h). HAADF STEM image (g,h) and line scan, displaying the chemical composition plot along the scan (i), and EDS mapping of UCNPs:$Er^{3+}/NaGdF_4$ core−shell−shell NPs.

for a broad range of biological applications. Additionally, Mn^{2+} ions also facilitate the decomposition of hydrogen peroxide (H_2O_2) into oxygen and water[19] by a Fenton-like mechanism.[9,20] The excessive consumption of oxygen and vascular shutdown during PDT, along with compromised microcirculation and reduced perfusion, lead to hypoxia, which diminishes the therapeutic efficacy and hinders the full therapeutic response.[1,6] Therefore, the hydrogenase-like catalytic property of Mn^{2+} ions may help relieve the hypoxia by breaking down H_2O_2 into oxygen, which is present in excessive amounts in the tumor microenvironment.[9,20]

Therefore, this work presents a systematic approach for the rational design and development of a core−shell−shell luminescent nanosensitizer based on $NaGdF_4:Yb^{3+},Tm^{3+},Ca^{2+}/NaGdF_4:Yb^{3+},Ca^{2+}/NaGdF_4:Mn^{2+}$ (Scheme 1) NPs with long-lived Mn^{2+} upconversion emission and enhanced $^1O_2$ generation. In this context, the Tm^{3+} ion was artfully introduced into the core of core−shell−shell NPs, whereas the Mn^{2+} ion was incorporated into the outer shell to

https://doi.org/10.1021/acsanm.4c04307
ACS Appl. Nano Mater. 2024, 7, 21104−21113

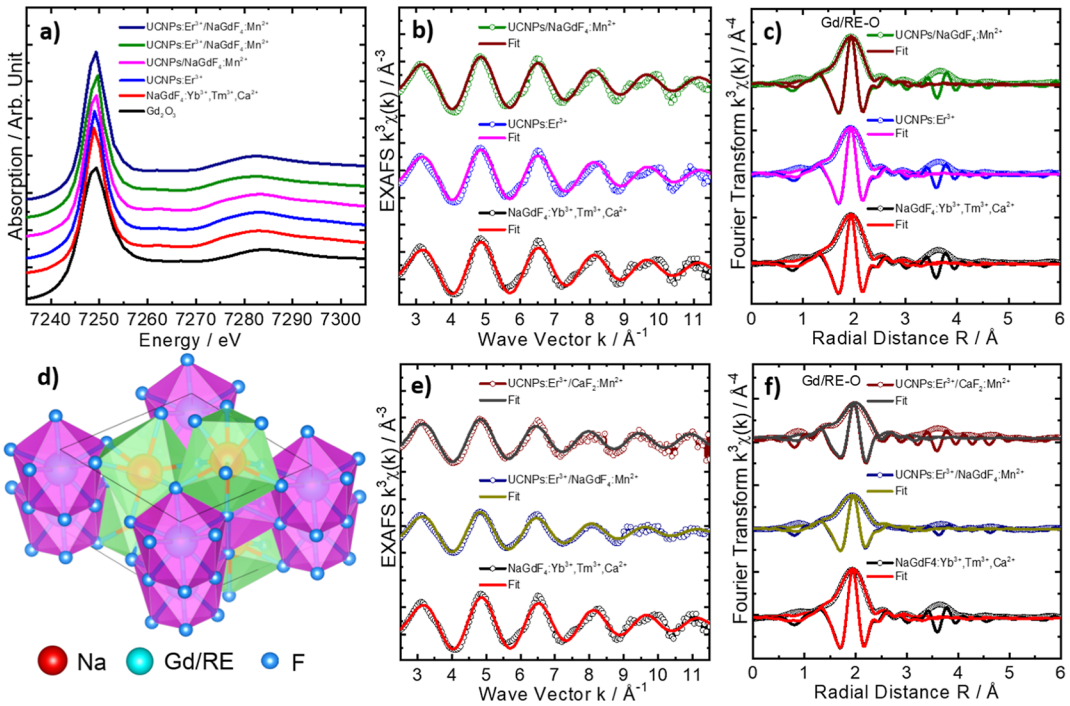

Figure 2. Normalized Gd L_3-edge (7243 eV) XANES spectra (a), with the k^3-weighted EXAFS signals (left) and the respective Fourier transforms (right) with best fits at the Gd L_3-edge (7243 eV), showing both the amplitude and the real parts of the Fourier transforms of $\chi(k)$ and fits for the $NaGdF_4$:Yb^{3+},Tm^{3+},Ca^{2+} core, UCNPs:Er^{3+}, and UCNPs/$NaGdF_4$:Mn^{2+} (b,c), as well as UCNPs:Er^{3+}/$NaGdF_4$:Mn^{2+} and UCNPs:Er^{3+}/CaF_2:Mn^{2+} (e,f) nanomaterials. The three-dimensional crystallographic structure (d) of all these nanomaterials.

achieve its long-lived upconversion emission and hydrogenase-like catalytic properties. An intermediate mediator active shell was grown to attain maximum energy transfer of $Yb^{3+} \rightarrow Tm^{3+}$ and prevent backward energy transfer from the Mn^{2+} to Tm^{3+} ions. The NPs exhibited a broad range of multicolored emissions across the UV−visible region. The emission spectra of NPs were fine-tuned to coincide with the absorption spectra of Rose Bengal (RB) through the incorporation of Er^{3+} ions at the inner shell of nanocrystals, thereby facilitating the architecting of RB-conjugated nanosensitizer for $^1O_2$ generation.

2. RESULTS AND DISCUSSION

The rational design of core−shell−shell NPs (Scheme 1a) featuring efficient long-lived Mn^{2+} emission was accomplished by energy migration from the Tm^{3+} doped in the core to the Mn^{2+} photoemitter in the outer shell, using Gd^{3+} as a mediator[15,16] (Scheme 1b). To validate the hypothesis, we initially synthesized the $NaGdF_4$:Yb^{3+},Tm^{3+},Ca^{2+} core nanomaterials, followed by surface passivation with the $NaGdF_4$:Yb^{3+},Ca^{2+} layer to produce the $NaGdF_4$:Yb^{3+},Tm^{3+},Ca/$NaGdF_4$:Yb^{3+},Ca^{2+} core−shell NPs. The core−shell NPs were subsequently further coated with a series of $NaGdF_4$ matrices doped with a fixed concentration of Mn^{2+} (30 mol %) with varying amounts of xCa^{2+} ions (x = 0, 12, 24, 36, 48, 60, and 70 mol %), respectively, resulting in multilayered $NaGdF_4$:Yb^{3+},Tm^{3+},Ca^{2+}/$NaGdF_4$:Yb^{3+},Ca^{2+}/$NaGdF_4$:xCa^{2+},Mn^{2+} (x: 0, 12, 24, 36, 48, 60, and 70 mol %) NPs.

In order to diversify the upconversion emission, an Er^{3+} activator was incorporated into the intermediate layer to produce $NaGdF_4$:Yb^{3+},Tm^{3+},Ca^{2+}/$NaGdF_4$:Yb^{3+},Er^{3+},Ca^{2+}, which was subsequently passivated with outer layers of $NaGdF_4$:Mn^{2+} and CaF_2:Mn^{2+}, yielding $NaGdF_4$:Yb^{3+},Tm^{3+},Ca^{2+}/$NaGdF_4$:Yb^{3+},Er^{3+},Ca^{2+}/$NaGdF_4$:Mn^{2+} and $NaGdF_4$:Yb^{3+},Tm^{3+},Ca^{2+}/$NaGdF_4$:Yb^{3+},Er^{3+},Ca^{2+}/CaF_2:Mn^{2+} core−shell−shell NPs, respectively. The obtained series of upconversion materials were labeled as per the following Table 1 for ease of reference, which is consistently used throughout the article. It is noteworthy that the amount of Mn^{2+} is kept constant at 30%; therefore, Mn^{2+} ions are mentioned in all of the formulas without specifying its concentration each time.

To develop luminescent nanosensitizers (Scheme 1a), UCNPs:Er^{3+}/$NaGdF_4$:Mn^{2+} and UCNPs:Er^{3+}/$NaGdF_4$ NPs were rendered water-soluble by ligand exchange. This procedure involved treating with nitronium tetrafluoroborate (NO_2BF_4), followed by overcoating with polyethyleneimine (PEI), resulting in NPs-PEI. The NPs-PEI were subsequently conjugated with RB to produce UCNPs-PEI-RB, which was verified via Fourier transform infrared (FTIR) spectroscopy analysis (Figure S1).

The X-ray diffraction (XRD) patterns of the obtained UCNPs (Figure S2) exhibited similar diffraction peaks to those reported for $NaGdF_4$:Yb^{3+},Er^{3+} by our research group.[11] Besides, UCNPs/$NaGdF_4$:xCa^{2+},Mn^{2+} (x = 12, 24, and 36 mol %) (Figure S3) experienced no observable phase transformation in the XRD patterns after doping the outer shell with Ca up to 36%. However, characteristic diffraction patterns corresponding to CaF_2 appeared in the XRD data of UCNPs/$NaGdF_4$: xCa^{2+},Mn^{2+} (x = 48, 60, and 70 mol %), following an increase in the amount of Ca above 48%, indicating the successful passivation of core−shell NPs by CaF_2 in the UCNPs/CaF_2:Mn^{2+} (Figure S3). The XRD patterns of CaF_2 exhibited a fluorite-type cubic structure, where Ca is located at the cubic closed packed (ccp) sites and F atoms occupy all the tetrahedral interstitial sites with the $Fm\bar{3}m$ space group (JCPDS: 35-0816).[21]

https://doi.org/10.1021/acsanm.4c04307
ACS Appl. Nano Mater. 2024, 7, 21104−21113

Table 2. EXAFS Fitting Parameters, Including the Coordination Number (N), Mean Coordination Shell Radii (R), Mean Square Relative Displacements or Debye−Waller Factor (σ^2), Amplitude Reduction Factor (S_0^2), Photoelectron Energy (E_0), and Goodness of Fit (R_{factor}) for the Core, Core−Shell, and Core−Shell−Shell UCNPs

material	bond type	N	R (Å)	σ^2 (Å^2)	S_0^2	E_0 (eV)	R_{factor}
$NaGdF_4$:Yb^{3+},Tm^{3+},Ca^{2+}	Gd−F	3	2.237 ± 0.017	0.0058 ± 0.0032	1	0.065	0.0036
	Gd−F	3	2.331 ± 0.018	0.0031 ± 0.0009	1	0.065	0.0036
	Gd−F	3	2.401 ± 0.018	0.0031 ± 0.0009	1	0.065	0.0036
UCNPs:Er^{3+}	Gd−F	3	2.256 ± 0.029	0.0105 ± 0.0063	1	0.065	0.0032
	Gd−F	3	2.315 ± 0.032	0.0040 ± 0.0010	1	0.065	0.0032
	Gd−F	3	2.401 ± 0.032	0.0040 ± 0.0010	1	0.065	0.0032
UCNPs/$NaGdF_4$:Mn^{2+}	Gd−F	3	2.239 ± 0.018	0.0068 ± 0.0035	1	0.065	0.0038
	Gd−F	3	2.333 ± 0.019	0.0034 ± 0.0009	1	0.065	0.0038
	Gd−F	3	2.402 ± 0.019	0.0034 ± 0.0009	1	0.065	0.0038
UCNPs:Er^{3+}/$NaGdF_4$:Mn^{2+}	Gd−F	3	2.288 ± 0.046	0.0216 ± 0.0097	1	0.065	0.0042
	Gd−F	3	2.340 ± 0.017	0.0089 ± 0.0013	1	0.065	0.0042
	Gd−F	3	2.382 ± 0.017	0.0089 ± 0.0013	1	0.065	0.0042
UCNPs:Er^{3+}/CaF_2:Mn^{2+}	Gd−F	3	2.217 ± 0.012	0.0081 ± 0.0029	1	0.065	0.0057
	Gd−F	3	2.371 ± 0.012	0.0050 ± 0.0011	1	0.065	0.0057
	Gd−F	3	2.401 ± 0.012	0.0050 ± 0.0011	1	0.065	0.0057

The transmission electron microscopy (TEM) images revealed that the $NaGdF_4$:Yb^{3+},Tm^{3+},Ca^{2+} is composed of spherical and nearly uniform NPs (Figure 1a,b) with an average diameter of 10.84 ± 0.41 nm. However, after growing a $NaGdF_4$:Yb^{3+},Er^{3+},Ca^{2+} shell over the $NaGdF_4$:Yb^{3+},Tm^{3+},Ca^{2+} core, the obtained UCNPs:Er^{3+} core−shell NPs exhibited spherical and monodisperse features (Figure 1c,d) with an average size of 22.13 ± 0.95 nm, suggesting the formation of core−shell NPs. Interestingly, the TEM analysis revealed a beautiful daisy flower-like morphology for the UCNPs:Er^{3+}/$NaGdF_4$ NPs (Figure 1e−h) with an average size of 69.22 ± 2.07 nm. The emergence of these unique morphologies, even under identical conditions, was unexpected and remains unclear. However, after doping the outer shell of UCNPs:Er^{3+}/$NaGdF_4$ NPs with 30% Mn^{2+}, a notable reduction in the size of UCNPs:Er^{3+}/$NaGdF_4$:Mn^{2+} (Figure S4) was observed, displaying an average diameter of 56.96 ± 1.81 nm (Figure S4).

The chemical composition of the NPs was probed by energy-dispersive X-ray spectroscopy (EDS) elemental mapping (Figure 1), with bright field (BF) and high-angle annular dark field (HAADF) in the scanning transmission electron microscopy (STEM) mode, using a state-of-the-art high-resolution TEM-Titan Themis Cube microscope. The elemental mapping validated the uniform localization of all of the elements (F, Na, Ca, Gd, Er, Tm, and Yb) for the UCNPs:Er^{3+}/$NaGdF_4$ core−shell−shell NPs (Figure 1). A similar elemental composition was also validated by the selective line scan of the HADDF image, as depicted in the elemental composition's plot (Figure 1i). Furthermore, the BF and HAADF images of UCNPs:Er^{3+}/CaF_2:Mn^{2+} NPs (Figure S5) presented comparatively smaller and spherical morphology with an average diameter of 22.67 ± 71 nm. However, the elemental mapping and specific area line scan also localized the uniform distribution of all the elements (F, Na, Ca, Mn, Gd, Er, Tm, and Yb) in the lattice of the core−shell−shell NPs.

2.1. Probing the Local Atomic Structure of Nanosensitizers by X-ray Absorption Fine Structure. The Gd L_3-edge (7243 eV) X-ray absorption near-edge spectroscopy (XANES) spectra of the upconversion nanomaterials manifested a high-intensity white line peak at ∼7249 eV, from the $2p_{3/2}$ initial state to the 5d final state electronic transition of the trivalent Gd^{3+} ion (Figure 2a). It is hypothesized that the total area under the white line peak for the Gd L_3-edge spectrum represents the number of empty 5d states.[22,23] Therefore, the NPs exhibited a white line peak area approximately similar to that of the Gd_2O_3 reference material, suggesting a comparable electronic configuration and consequential empty 5d levels (Figure 2a). However, the change in the postedge region of the upconversion nanomaterials, especially the broad peak in the energy range of 7270−7300 eV, corresponds to the first extended X-ray absorption fine structure (EXAFS) oscillation, which originates from the single scattering contribution of nearest neighboring atoms. This manifests different local chemical environments for the core and core−shell NPs when compared to the reference Gd_2O_3. Nevertheless, the overall similarity in the postedge features of the core and core−shell upconversion nanomaterials validates the similar local geometry of the trivalent Gd^{3+} ion, as expected.

2.1.1. Quantitative EXAFS Analysis. The inclusive insights into the local atomic structure of the core and core−shell−shell upconversion nanomaterials were gained by a quantitative nonlinear fit to their Gd L_3-edge (7243 eV) EXAFS data (Section S8), using Artemis from the Demeter[24] package. The fit was performed in R-space, using a previously reported hexagonal crystal structure of the β-$NaGdF_4$ with lattice parameters of $a = b = 6.0304$ Å and $c = 6.9957$ Å and a space group of $P6(174)$ to derive the effective backscattering amplitudes and phase shifts in Artemis, resulting in the generation of various scattering paths (eq S1). The experimental EXAFS data, spanning an R-space interval from 1.0 to 2.9 Å with the Hanning window and a k range of 3−11.3 Å^{-1}, were used in the best fit analyses. The initial three high-ranking single scattering paths of Gd−F bond pairs were included in the fit. The passive electrons reduction factor S_0^2 and energy shift E_0 were set similar and constrained for all the paths in the fit of all the NPs, whereas the mean square relative displacement σ^2 and interatomic distance R were refined relatively to get the best fit result.

The quantitative Gd L_3-edge EXAFS analyses manifested similar experimental and theoretical k^3-weighted EXAFS signals (Figure 2b,e), indicating a similar local structure for the $NaGdF_4$:Yb^{3+},Tm^{3+},Ca^{2+} core, core−shell, and core-

https://doi.org/10.1021/acsanm.4c04307
ACS Appl. Nano Mater. 2024, 7, 21104−21113

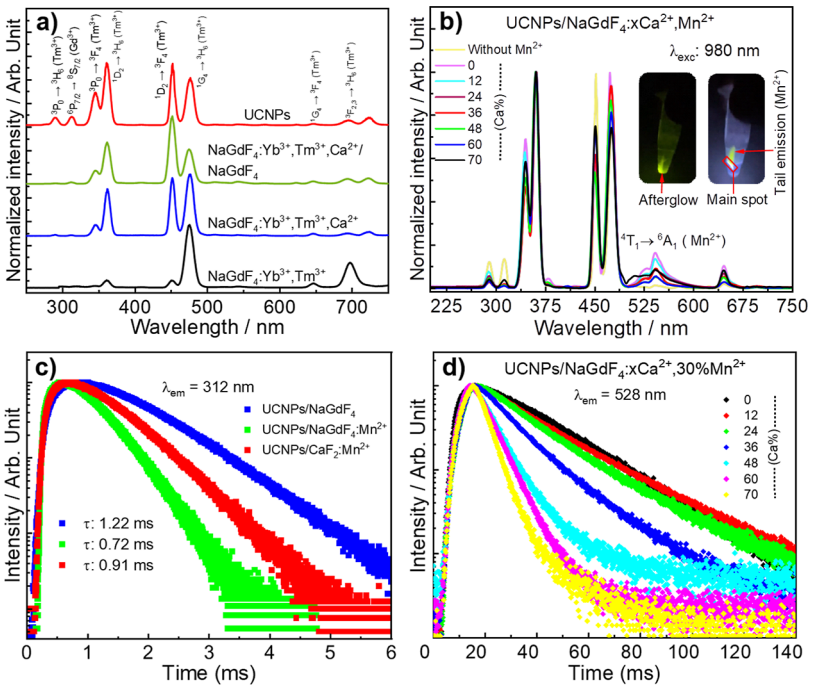

Figure 3. Overview of PL spectra of $NaGdF_4:Yb^{3+},Tm^{3+}$, $NaGdF_4:Yb^{3+},Tm^{3+},Ca^{2+}$ core, $NaGdF_4:Yb^{3+},Tm^{3+},Ca^{2+}/NaGdF_4$, and $NaGdF_4:Yb^{3+},Tm^{3+},Ca^{2+}/NaGdF_4:Yb^{3+},Ca^{2+}$ core−shell NPs (a) and $UCNPs/NaGdF_4:xCa^{2+},Mn^{2+}$ (b). Illustration of decay curves of UCNPs/$NaGdF_4$, $UCNPs/CaF_2:Mn^{2+}$, and $UCNPs/NaGdF_4:Mn^{2+}$ recorded at 311 nm from Gd^{3+} emission (c) and $UCNPs/NaGdF_4:xCa,Mn^{2+}$ recorded at 528 nm from Mn^{2+} emission (d). Visualization of green emission from Mn^{2+} (figure b inset): the main spot consisting of Tm^{3+} and Mn^{2+} emissions as well as a tail originating from Mn^{2+} emission and the afterglow of Mn^{2+}.

multishell NPs. The Fourier transform of the Gd L_3-edge EXAFS data (Figure 2c,f) displayed a dominant peak corresponding to the Gd−F bond pairs. The best fit results revealed nine backscattering fluorine atoms (Table 2), including the first three single scattering paths (1.0−3.9 Å) around the Gd absorbing atom, thus confirming the hexagonal local crystal lattice of β-NaGd/REF_4 for all core and core-multishell NPs (Figure 2d).

It is noteworthy that the interatomic distances of the Gd−F bonds in NP lattices remained largely unchanged, with only slight fluctuation in values among the core−shell NPs (Table 2). This consistency is due to the similar size of RE^{3+} ions substituting for the Gd^{3+} sites. However, values of σ^2 (Debye−Waller factors) were increased for $UCNPs:Er^{3+}$, $UCNPs/NaGdF_4:Mn^{2+}$, $UCNPs:Er^{3+}/NaGdF_4:Mn^{2+}$, and $UCNPs:Er^{3+}/CaF_2:Mn^{2+}$ compared to those for $NaGdF_4:Yb^{3+},Tm^{3+},Ca^{2+}$, suggesting an introduction of structural disorder in the hexagonal β-NaGd/REF_4 lattice following the deposition of the additional shell and doping with Mn^{2+} and Ca^{2+} ions. Furthermore, Mn K-edge (6539 eV) XAFS data (Figure S6) of the $UCNPs:Er^{3+}/NaGdF_4:Mn^{2+}$ revealed mixed occupancy of Mn^{2+}/Gd^{3+} at the cation sites in the β-NaGd/REF_4 lattice. The slight shift toward a lower interatomic distance of Mn−F than that of Gd−F is attributed to the smaller ionic radius of Mn^{2+} relative to that of the Gd^{3+} ions. The Mn K-edge XAFS data (Figure S6) of the $UCNPs:Er^{3+}/CaF_2:Mn^{2+}$ clearly demonstrated that Mn^{2+} occupies two different sites, likely within the β-NaGd/REF_4 and CaF_2 lattices. Nevertheless, it can be deduced from the quantitative XAFS analysis that the Gd^{3+} is located in the hexagonal β-$NaGdF_4$ lattice for the core and bilayer/multilayer core−shell NPs, irrespective of additional surface coating, whereas Mn^{2+} occupies two different local sites in the core−multishell lattice of the $UCNPs:Er^{3+}/CaF_2:Mn^{2+}$ NPs.

2.2. PL Study. In this study, we devised a strategy of energy migration involving $Yb^{3+} \rightarrow Tm^{3+} \rightarrow Gd^{3+} \rightarrow Mn^{2+}$ to achieve long-lived Mn^{2+} upconversion emission in core−multishell nanocrystals. For this purpose, Tm^{3+} ions were used as photon emitters, which provided multiple emissions paths ranging from the UV to visible wavelengths, and the Gd matrix was employed as an energy mediator[15,16] because of its ability to exhibit emission peaks around 311 nm. The energy of the excited state of the Gd^{3+} ion was subsequently transferred to Mn^{2+} emitter ions via an energy migration mechanism.[15,16] Gd^{3+} upconversion emission (~311 nm, $^6P_{7/2} \rightarrow {}^8S_{7/2}$) was achieved by strategically designing and regulating the composition of $NaGdF_4:Yb^{3+},Tm^{3+},Ca^{2+}/NaGdF_4:Yb^{3+},Ca^{2+}$ through the incorporation of the Ca^{2+} (10%) in the core and shell of NPs, leading to a significant increase in Gd^{3+} emission intensity compared to that of $NaGdF_4:Yb^{3+},Tm^{3+}$ NCs (Figure 3a). The PL spectrum of $NaGdF_4:Yb^{3+},Tm^{3+}$ (Figure 3a, black line) exhibited a dominant emission peak at ~475 nm assigned to the $^1G_4 \rightarrow {}^3H_6$ transition of the Tm^{3+} ion, as well as lower emission intensity bands at 363 nm ($^1D_2 \rightarrow {}^3H_6$), 454 nm ($^1D_2 \rightarrow {}^3F_4$), 646 nm ($^1G_4 \rightarrow {}^3F_4$), and 696 nm ($^3F_{2,3} \rightarrow {}^3H_6$). However, the emission intensity of bands at 345, 363, and 454 nm experienced a significant increase in $NaGdF_4:Yb^{3+},Tm^{3+},Ca^{2+}$ (Figure 3a, blue line) following the incorporation of Ca^{2+} when compared to those observed in the $NaGdF_4:Yb^{3+},Tm^{3+}$ nanomaterial (Figure 3a, black line). It is known that the mechanism governing the excited-state population and transition probabilities in rare earth materials are greatly influenced by the choice of the host matrix and the crystal field effect, favoring certain emission bands over the other. Therefore, the optimal enhancement of luminescence

https://doi.org/10.1021/acsanm.4c04307
ACS Appl. Nano Mater. 2024, 7, 21104−21113

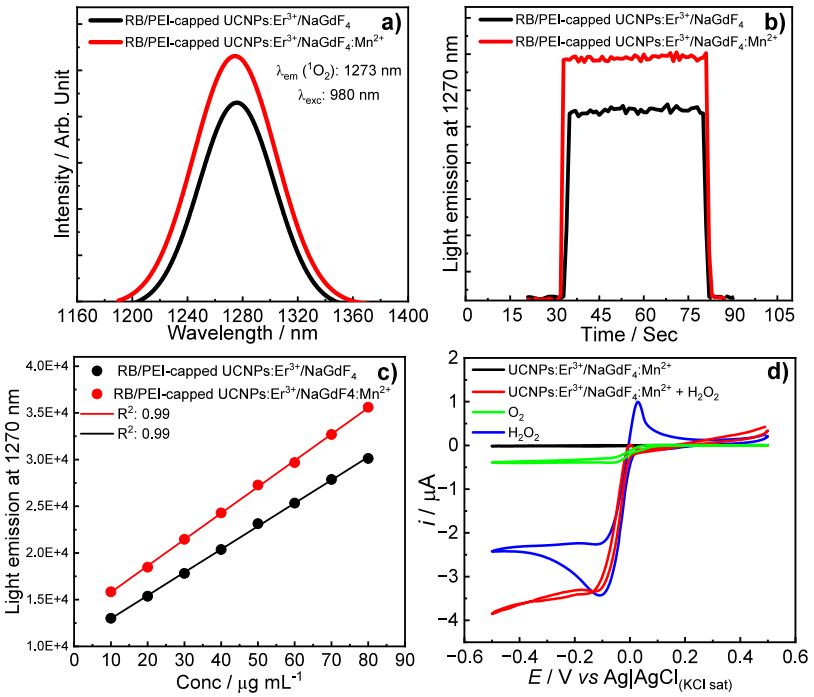

Figure 4. Phosphorescence spectra of $^1O_2$ generated by UCNPs/PEI-RB and UCNPs:Mn^{2+}/PEI-RB: (a) comparative analysis of current density/signal associated with monomolecular oxygen at 1273 nm produced by RB/PEI-capped UCNPs:Er^{3+}/$NaGdF_4$ and RB/PEI-capped UCNPs:Er^{3+}/$NaGdF_4$:Mn^{2+} (b), increase in signal intensity with the increase in the concentration of the nanosensitizer (c), and cyclic voltammetry response to H_2O_2 decomposition by the peroxidase-like catalytic properties of Mn^{2+} and production of molecular oxygen using UCNPs:Er^{3+}/$NaGdF_4$:Mn^{2+} NPs (d).

intensity in the UV−vis region was achieved by incorporating 10% Ca^{2+} in the core and shell of UCNPs (Figure 3a). Thus, the changes in the chemical environment at around Tm^{3+} ions, induced by Ca through the crystal field modification, lattice distortion, or defect reduction, might be responsible for the alteration in emission spectral profiles.[7]

Additionally, the upconversion emission intensity was enhanced especially in the UV region after cladding the $NaGdF_4$:Yb^{3+},Tm^{3+},Ca^{2+} core by the $NaGF_4$:Yb^{3+},Ca^{2+} shell (Figure 3a, red line). This optical feature can be attributed to an additional energy transfer from the Yb^{3+} sensitizer[25] to the Tm^{3+} ion as well as a decrease of the luminescence quenching by surface defects. It is because a higher amount of Yb^{3+} leads to increased cross-section absorption per particle, hence facilitating an enhanced energy transfer between Yb^{3+} and Tm^{3+} ions. The excited photons in the higher levels of Tm^{3+} in the $NaGdF_4$:Yb^{3+},Tm^{3+},Ca^{2+}/$NaGdF_4$:Yb^{3+},Ca^{2+} core−shell were subsequently migrated to Mn^{2+} ions through the Gd mediator in $NaGdF_4$:Yb^{3+},Tm^{3+},Ca^{2+}/$NaGdF_4$:Yb^{3+},Ca^{2+}/$NaGdF_4$:Mn^{2+} core−shell−shell NPs (Figure 3b). The emission profile of resulting NPs exhibited a broad emission band ranging from 500 to 600 nm, which was attributed to the radiative intraconfigurational $3d^5$ transition of Mn^{2+} [$^4T_1(^4G) \rightarrow {}^6A_1(^6S)$].[26] The intense green afterglow of Mn^{2+} can be visualized by the naked eye after the Tm^{3+} emission is ceased (Video S1 and inset of Figure 3b), which is consistent with the previously reported findings.[15,16] The phenomenon of energy migration to Mn^{2+} ions was accompanied by a significant decrease in the decay lifetime of Gd (311 nm, $^6P_{7/2} \rightarrow {}^8S_{7/2}$) (Figure 3c), suggesting the role of Gd^{3+} ions as a mediator. The energy transfer efficiency from Gd^{3+} to Mn^{2+} ions was calculated to be 48.98% for UCNPs/$NaGdF_4$:Mn^{2+} and 25.41% for UCNPs/CaF_2:Mn^{2+}. Furthermore, the role of Gd^{3+} ion as a mediator in the energy migration process toward Mn^{2+} was validated by gradually increasing the amount of Ca^{2+} in the outer shell while investigating its effect on the emission intensity and excited state lifetime of Mn^{2+} ions. The emission intensity of Mn^{2+} exhibited a steady decline accompanied by a shortening in the decay lifetime as the amount of Ca was increased in the outermost shell (Figure 3b,d), confirming the energy transfer from Gd^{3+} to Mn^{2+}.

To assess the effect of Mn^{2+} contents on Tm^{3+} emissions, luminescence decay curves (Figure S7) were recorded for the NPs both with and without Mn^{2+} ions at the excited states of the Tm^{3+} ion. The decay curves of Tm^{3+} ions showed minimal shortening, possibly due to quenching by Mn^{2+} ions at the interface.

To diversify the upconversion emission, Er^{3+} activator ions were incorporated into the intermediate layer of core−shell−shell NPs. Consequently, the PL spectra of resulting NPs exhibited additional narrow emission lines assigned to $^2H_{9/2} \rightarrow {}^4I_{15/2}$, $^2H_{11/2} \rightarrow {}^4I_{15/2}$, and $^4S_{3/2} \rightarrow {}^4I_{15/2}$ transitions of the Er^{3+} ions (Figure S8). However, the addition of the Er^{3+} ion led to a significant reduction in Tm^{3+} emission intensity, implying that most of the excitation photons absorbed by the shell resulted in emission relaxation from the Er^{3+} ion. The corresponding effect of Mn^{2+} contents on Er^{3+} emissions was measured by recording the luminescence decay curves at 523 and 542 nm for UCNPs:Er^{3+}/$NaGdF_4$ and UCNPs:Er^{3+}/$NaGdF_4$:Mn^{2+} NPs, respectively (Figure S9). The decay curves of Er^{3+} exhibited a slight enhancement, possibly attributed to the energy transferred from Mn^{2+} to Er^{3+} ions at the interface of shells.

2.3. Singlet Molecular Oxygen Generation. For singlet oxygen generation, UCNPs:Er^{3+}/$NaGdF_4$ and UCNPs:Er^{3+}/$NaGdF_4$:Mn^{2+} were selected as activator nanomaterials, and

https://doi.org/10.1021/acsanm.4c04307
ACS Appl. Nano Mater. 2024, 7, 21104−21113

RB was chosen as the molecular sensitizer of dioxygen. The absorption spectrum of RB overlapped very well with emission bands of Er^{3+} ions, which ensured that upconversion nanomaterials would effectively transfer energy to activate RB under excitation at 980 nm. The generation of $^1O_2$ by different nanosensitizers (RB/PEI-capped UCNPs:Er^{3+}/$NaGdF_4$ and RB/PEI-capped UCNPs:Er^{3+}/$NaGdF_4$:Mn^{2+}) was detected separately by recording the phosphorescence spectrum of $^1O_2$ at 1273 nm[1] and the phosphorescence kinetics[2] corresponding to the emission decay of $^1O_2$. The RB/PEI-capped UCNPs:Er^{3+}/$NaGdF_4$:Mn^{2+} nanosensitizers were observed to produce a higher amount of $^1O_2$ than RB/PEI-capped UCNPs:Er^{3+}/$NaGdF_4$, as is evident from the phosphorescence spectrum (Figure 4a) and phosphorescence kinetics (Figure 4b) of $^1O_2$ generated by RB/PEI-capped UCNPs:Er^{3+}/$NaGdF_4$:Mn^{2+}, which exhibited higher emission intensity than that of RB/PEI-capped UCNPs:Er^{3+}/$NaGdF_4$. Both the nanosensitizers demonstrated an efficient production of $^1O_2$ and its amount enhanced with increasing the respective amount of nanosensitizers, i.e., 10 to 80 μg/mL, as shown in Figure S10. The enhanced production of $^1O_2$ by RB/PEI-capped UCNPs:Er^{3+}/$NaGdF_4$:Mn^{2+} can be attributed to an efficient energy transfer to the RB sensitizer via Förster resonance energy transfer due to the longer lifetime of the Er^{3+} ion and comparatively smaller size of the NPs. RB/PEI-capped UCNPs:Er^{3+}/$NaGdF_4$:Mn^{2+} (5 μg/mL, comprising 3 μg of RB linked to 2 μg of NPs), under very low power laser irradiation (2 mW cm^{-2}), demonstrated superior singlet molecular oxygen production, yielding 0.39 μM $^1O_2$, compared to a pure chemical source of $^1O_2$, $DHPNO_2$ (90 μg/mL) (Figure S11), which generated 0.24 μM $^1O_2$.

However, in the presence of chemical trapping using anthracene-9,10-divinylsulfonate (AVS),[4] the signal from $^1O_2$ experienced a significant decrease (Figure S12), indicating the occurrence of a reaction between singlet molecular oxygen and anthracene derivative. A similar reduction in $^1O_2$ production was observed when the nanosensitizer was introduced to sodium azide (NaN_3),[4] known for its ability to quench $^1O_2$ physically. The reduction in the signal became more evident with the increase in the concentration of NaN_3 (Figure S12).

Mn (II) has been reported to catalytically decompose H_2O_2 into O_2 and H_2O, mimicking hydrogenase-like activities, which is significantly important for alleviating the hypoxia in tumor environments.[27] Therefore, the oxygen production capability of UCNPs:Er^{3+}/$NaGdF_4$:Mn^{2+} was investigated in the presence of H_2O_2 by an electrochemical experiment utilizing a nanoporous gold microelectrode. The electrode was first calibrated separately for H_2O_2 and O_2 in individual experiments. The blue curve in Figure 4d shows the voltammogram recorded in a H_2O_2 solution, displaying distinct peaks for the reduction (at −0.1 V) and oxidation (at 0.03 V) processes. In contrast, the voltammogram of O_2 (Figure 4d, green curve) reveals only one cathodic process at a similar potential with no corresponding anodic component, which is an important feature to distinguish both molecules.

However, after adding UCNPs-Er^{3+}/$NaGdF_4$:Mn^{2+} to the H_2O_2 solution, the voltammogram (Figure 4d, red curve) revealed no anodic peak, indicating the conversion of all H_2O_2 to O_2. Notably, the new voltammogram (Figure 4d, red curve) closely resembled that for dissolved O_2 but exhibited significantly higher steady-state current, which was attributed to the decomposition of H_2O_2 and generation of O_2.

3. CONCLUSIONS

The study presents the design and fabrication of core−multishell upconversion nanomaterials toward achieving long-lived emission of Mn^{2+} and subsequently development of the RB/PEI-capped UCNPs:Er^{3+}/$NaGdF_4$:Mn^{2+} nanosensitizer for enhanced $^1O_2$ generation. The XRD patterns of core and multilayered core−shell−shell NPs confirmed the hexagonal phase of β-$NaGdF_4$ with the $P\bar{6}(174)$ space group, corroborated through local atomic structure order by quantitative EXAFS analysis. The TEM and STEM analysis demonstrated spherical and nearly uniform morphology for core nanocrystals; however, interestingly, the $NaGdF_4$:Yb^{3+},Tm^{3+},Ca^{2+}/$NaGdF_4$:Yb^{3+},Er^{3+},Ca^{2+}/$NaGdF_4$ multilayered core−shell−shell NPs revealed exquisite daisy flower-like morphology. Meanwhile, the findings suggest that incorporating a suitable amount of Ca in the core and shell of NPs can enhance the emission intensity of Tm^{3+} ions in the higher energy (UV) region, leading to improved emission of Gd^{3+} ions due to the efficient energy transfer from Tm^{3+} ions. The energy of the excited state of the Gd^{3+} ions was subsequently transferred to Mn^{2+} ions doped in the outer shell of multilayered core−shell−shell NPs, resulting in long-lived Mn^{2+} upconversion emission. The Mn^{2+} ions were intentionally incorporated in the outer shell of multilayered core−shell−shell NPs to serve dual functions: (i) demonstrating prolonged Mn^{2+} upconversion emission, and (ii) performing hydrogenase-like catalytic properties for the decomposition H_2O_2 into oxygen and reactive oxygen species. The rational design of the nanosensitizer was based on incorporating the Er^{3+} ions into the intermediate shell of multilayered core−shell−shell NPs followed by conjugating with RB, which produced efficient $^1O_2$ at a very low concentration (5 μg) under a low power irradiation (2 mW cm^{-2}). Hence, these findings may contribute to advancing the development of versatile nanosensitizers featuring multimodal bioimaging and therapeutic functionalities, including $^1O_2$ generation and alleviating the hypoxia by the decomposition of H_2O_2, which is present in higher amounts in the tumor microenvironment, into molecular oxygen.

■ ASSOCIATED CONTENT

Supporting Information

The Supporting Information is available free of charge at https://pubs.acs.org/doi/10.1021/acsanm.4c04307.

Materials and methods, FTIR, XRD patterns, high-resolution TEM, EXAFS, PL spectra, and singlet oxygen characterization (PDF)

Visualization of green emission from Mn^{2+} after the Tm^{3+} emission is ceased (MP4)

■ AUTHOR INFORMATION

Corresponding Authors

Zahid U. Khan − *Department of Biochemistry, Institute of Chemistry, University of São Paulo (USP), 05508-000 São Paulo-SP, Brazil; Research Centre for Greenhouse Gas Innovation, University of Sao Paulo (USP), 05508-030 São Paulo-SP, Brazil;* orcid.org/0000-0003-1529-0832; Email: zahid@iq.usp.br

Hermi F. Brito − *Department of Fundamental Chemistry, Institute of Chemistry, University of São Paulo (USP), 05508-000 São Paulo-SP, Brazil;* orcid.org/0000-0002-9876-4441; Email: hefbrito@iq.usp.br

https://doi.org/10.1021/acsanm.4c04307
ACS Appl. Nano Mater. 2024, 7, 21104−21113

Paolo Di Mascio − *Department of Biochemistry, Institute of Chemistry, University of São Paulo (USP), 05508-000 São Paulo-SP, Brazil;* orcid.org/0000-0003-4125-8350; Email: pdmascio@iq.usp.br

Authors

Latif U. Khan − *Department of Biochemistry, Institute of Chemistry, University of São Paulo (USP), 05508-000 São Paulo-SP, Brazil; Synchrotron-light for Experimental Science and Applications in the Middle East (SESAME), Allan 19252, Jordan;* orcid.org/0000-0002-3535-7099

Fernanda M. Prado − *Department of Biochemistry, Institute of Chemistry, University of São Paulo (USP), 05508-000 São Paulo-SP, Brazil;* orcid.org/0000-0003-4458-4354

Iram Gul − *Research Centre for Greenhouse Gas Innovation, University of Sao Paulo (USP), 05508-030 São Paulo-SP, Brazil*

Thiago Lopes − *Research Centre for Greenhouse Gas Innovation, University of Sao Paulo (USP), 05508-030 São Paulo-SP, Brazil*

Leonardo M. A. Ribeiro − *Department of Fundamental Chemistry, Institute of Chemistry, University of São Paulo (USP), 05508-000 São Paulo-SP, Brazil;* orcid.org/0000-0003-2508-5007

Mauro Bertotti − *Department of Fundamental Chemistry, Institute of Chemistry, University of São Paulo (USP), 05508-000 São Paulo-SP, Brazil;* orcid.org/0000-0001-9566-7577

Magnus Gidlund − *Institute of Biomedical Sciences-IV, University of São Paulo (USP), 05508-000 São Paulo-SP, Brazil;* orcid.org/0000-0003-2047-1136

Complete contact information is available at: https://pubs.acs.org/10.1021/acsanm.4c04307

Author Contributions

The manuscript was written through the contributions of all authors. All authors have approved the final version of the manuscript. Z.U.K.: conceptualization, experimental, methodology, investigation, formal analysis, data curation, validation, visualization, writing—original draft, and writing—review and editing. L.U.K.: conceptualization, experimental, methodology, investigation, data curation, software, writing—original draft, and writing—review and editing. F.M.D. and L.M.A.: methodology, experimental, and data curation. M.A.G. and H.F.B.: conceptualization, project administration, visualization, writing—review and editing, supervision, and resources. T.L., I.G., and M.B.: review and editing and resources. P.D.M. conceptualization, formal analysis, funding acquisition, investigation, methodology, project administration, resources, supervision, visualization, writing—original draft, and writing—review and editing.

Funding

The Article Processing Charge for the publication of this research was funded by the Coordination for the Improvement of Higher Education Personnel - CAPES (ROR identifier: 00x0ma614).

Notes

The authors declare no competing financial interest.

■ ACKNOWLEDGMENTS

The authors acknowledge the financial support from the Fundação de Amparo à Pesquisa do Estado de São Paulo (FAPESP) (Z.U.K., no. 2021/00356-6, H.F.B., no. 2021/08111-2). We also extend our gratitude to the Brazilian Nanotechnology National Laboratory (LNNano), part of the Brazilian Center for Research in Energy and Materials (CNPEM) for high-resolution TEM images and EDS elemental mapping (Proposal no. 20230320) and the BM08-XAFS/XRF Beamline of SESAME synchrotron light source for XAFS data measurements. P.D.M. acknowledge the support of the Brazilian research funding institutions, FAPESP CEPID Redoxoma (no. 2013/07937-8), Conselho Nacional de Desenvolvimento Científico e Tecnológico (CNPq no. 304350/2023-0, H.F.B., no. 308872/2022-3), CAPES (Coordenação de Aperfeiçoamento de Pessoal de Nível Superior), PRPUSP (Pro-Reitoria de Pesquisa da Universidade de São Paulo) (NAP Redoxoma (no. 2011.1.9352.1.8), and the John Simon Guggenheim Memorial Foundation. We would like to acknowledge Stella Boutris Jayme for preparing the $DHPNO_2$ and Marisa Helena Gennari de Medeiros for characterizing it.

■ REFERENCES

(1) Khan, Z. U.; Khan, L. U.; Brito, H. F.; Gidlund, M.; Malta, O. L.; Di Mascio, P. Colloidal Quantum Dots as an Emerging Vast Platform and Versatile Sensitizer for Singlet Molecular Oxygen Generation. *ACS Omega* **2023**, *8* (38), 34328−34353.

(2) Khan, Z. U.; Khan, L. U.; Uchiyama, M. K.; Prado, F. M.; Faria, R. L.; Costa, I. F.; Miyamoto, S.; Araki, K.; Gidlund, M.; Brito, H. F.; Di Mascio, P. Singlet Molecular Oxygen Generation via Unexpected Emission Color-Tunable CdSe/ZnS Nanocrystals for Applications in Photodynamic Therapy. *ACS Appl. Nano Mater.* **2023**, *6* (5), 3767−3780.

(3) Di Mascio, P.; Martinez, G. R.; Miyamoto, S.; Ronsein, G. E.; Medeiros, M. H. G.; Cadet, J. Singlet Molecular Oxygen Reactions with Nucleic Acids, Lipids, and Proteins. *Chem. Rev.* **2019**, *119* (3), 2043−2086.

(4) Nascimento, R. O.; Prado, F. M.; de Medeiros, M. H. G.; Ronsein, G. E.; Di Mascio, P. Singlet Molecular Oxygen Generation in the Reaction of Biological Haloamines of Amino Acids and Polyamines with Hydrogen Peroxide. *Photochem. Photobiol.* **2023**, *99* (2), 661−671.

(5) Juengpanich, S.; Li, S.; Yang, T.; Xie, T.; Chen, J.; Shan, Y.; Lee, J.; Lu, Z.; Chen, T.; Zhang, B.; Cao, J.; Hu, J.; Yu, J.; Wang, Y.; Topatana, W.; Gu, Z.; Cai, X.; Chen, M. Pre-Activated Nanoparticles with Persistent Luminescence for Deep Tumor Photodynamic Therapy in Gallbladder Cancer. *Nat. Commun.* **2023**, *14* (1), 5699.

(6) Chen, Y.; Yang, Y.; Du, S.; Ren, J.; Jiang, H.; Zhang, L.; Zhu, J. Mitochondria-Targeting Upconversion Nanoparticles@MOF for Multiple-Enhanced Photodynamic Therapy in Hypoxic Tumor. *ACS Appl. Mater. Interfaces* **2023**, *15* (30), 35884−35894.

(7) Dubey, N.; Chandra, S. Upconversion Nanoparticles: Recent Strategies and Mechanism Based Applications. *J. Rare Earths* **2022**, *40* (9), 1343−1359.

(8) Zhang, Z.; Han, Q.; Lau, J. W.; Xing, B. Lanthanide-Doped Upconversion Nanoparticles Meet the Needs for Cutting-Edge Bioapplications: Recent Progress and Perspectives. *ACS Mater. Lett.* **2020**, *2* (11), 1516−1531.

(9) Li, Y.; Chen, G. Upconversion Nanoparticles for Cancer Therapy. *Adv. NanoBiomed Res.* **2022**, *2* (12), 2200092.

(10) Feng, R.; Li, G.; Ko, C. N.; Zhang, Z.; Wan, J. B.; Zhang, Q. W. Long-Lived Second Near-Infrared Luminescent Probes: An Emerging Role in Time-Resolved Luminescence Bioimaging and Biosensing. *Small Struct.* **2023**, *4* (2), 2200131.

(11) Khan, L. U.; Khan, Z. U.; Rodrigues, R. V.; da Costa, L. S.; Gidlund, M.; Brito, H. F. Synthesis and Characterization of Tunable Color Upconversion Luminescence β-$NaGdF_4$:Yb^{3+},Er^{3+} Nanoparticles. *J. Mater. Sci.: Mater. Electron.* **2019**, *30* (18), 16856−16863.

(12) Khan, L. U.; Da Silva, G. H.; De Medeiros, A. M. Z.; Khan, Z. U.; Gidlund, M.; Brito, H. F.; Moscoso-Londoño, O.; Muraca, D.;

Knobel, M.; Pérez, C. A.; Martinez, D. S. T. Fe_3O_4@SiO_2 Nanoparticles Concurrently Coated with Chitosan and GdOF:-Ce^{3+},Tb^{3+} Luminophore for Bioimaging: Toxicity Evaluation in the Zebrafish Model. *ACS Appl. Nano Mater.* **2019**, *2* (6), 3414−3425.
(13) Khan, L. U.; Khan, Z. U. Bifunctional Nanomaterials: Magnetism, Luminescence and Multimodal Biomedical Applications. In *Complex Magnetic Nanostructures*; Springer, Cham, 2017; pp 121−171..
(14) Khan, L. U.; Khan, Z. U. Rare Earth Luminescence: Electronic Spectroscopy and Applications. In *Handbook of Materials Characterization*, 2018; Springer, Cham..
(15) Liu, X.; Ji, Q.; Hu, Q.; Li, C.; Chen, M.; Sun, J.; Wang, Y.; Sun, Q.; Geng, B. Dual-Mode Long-Lived Luminescence of Mn^{2+}-Doped Nanoparticles for Multilevel Anticounterfeiting. *ACS Appl. Mater. Interfaces* **2019**, *11* (33), 30146−30153.
(16) Yan, L.; Wang, X.; An, Z.; Hu, Z.; Liu, H.; Xu, S.; Zhou, B. Enhancing Upconversion of Manganese through Spatial Control of Energy Migration for Multi-Level Anti-Counterfeiting. *Nanoscale* **2021**, *13* (33), 13995−14000.
(17) Shrivastava, N.; Khan, L. U.; Khan, Z. U.; Vargas, J. M.; Moscoso-Londoño, O.; Ospina, C.; Brito, H. F.; Javed, Y.; Felinto, M. C. F. C.; Menezes, A. S.; Knobel, M.; Sharma, S. K. Building Block Magneto-Luminescent Nanomaterials of Iron-Oxide/ZnS@LaF_3:Ce^{3+},Gd^{3+},Tb^{3+} with Green Emission. *J. Mater. Chem. C* **2017**, *5* (9), 2282−2290.
(18) Ceresa, L.; Chavez, J.; Kitchner, E.; Kimball, J.; Gryczynski, I.; Gryczynski, Z. Imaging and Detection of Long-Lived Fluorescence Probes in Presence of Highly Emissive and Scattering Background. *Exp. Biol. Med.* **2022**, *247* (20), 1840−1851.
(19) Wekesa, M.; Ni, Y. Further Understanding of the Chemistry of Manganese-Induced Peroxide Decomposition. *Can. J. Chem. Eng.* **2003**, *81* (5), 968−972.
(20) Fan, M.; Liu, Y.; Ren, Y.; Gan, L.; Yang, Y.; Wang, H.; Liao, Y.; Yang, X.; Zheng, C.; Wang, Q. Cascade Reaction of "Mn^{2+}-Catechol" Triggered by H_2O_2 to Integrate Firm Tumor Vessel Embolization and Hypoxic Response Relief. *Adv. Healthcare Mater.* **2022**, *11* (15), 1−13.
(21) Chen, X.; Jin, L.; Sun, T.; Kong, W.; Yu, S. F.; Wang, F. Energy Migration Upconversion in Ce(III)-Doped Heterogeneous Core−Shell−Shell Nanoparticles. *Small* **2017**, *13* (43), 1−8.
(22) Khan, L. U.; Khan, Z. U.; Blois, L.; Tabassam, L.; Brito, H. F.; Figueroa, S. J. A. Strategy to Probe the Local Atomic Structure of Luminescent Rare Earth Complexes by X-ray Absorption Near-Edge Spectroscopy Simulation Using a Machine Learning-Based PyFitIt Approach. *Inorg. Chem.* **2023**, *62* (6), 2738−2750.
(23) Khan, L. U.; Khan, Z. U.; Alzubi, R. I.; Umer, M. A.; Juwhari, K.; Harfouche, M.; Brito, H. F. Tracking Coordination Environment and Optoelectronic Structure of Eu^{3+} and Sm^{3+} Sites via X-ray Absorption Spectroscopy and X-ray Excited Optical Luminescence. *Mater. Today: Proc.* **2024**, 1−8.
(24) Ravel, B.; Newville, M. ATHENA, ARTEMIS, HEPHAESTUS: Data Analysis for X-ray Absorption Spectroscopy Using IFEFFIT. *J. Synchrotron Radiat.* **2005**, *12* (4), 537−541.
(25) Dawson, P.; Romanowski, M. Excitation Modulation of Upconversion Nanoparticles for Switch-like Control of Ultraviolet Luminescence. *J. Am. Chem. Soc.* **2018**, *140* (17), 5714−5718.
(26) Liu, X.; Wang, Y.; Li, X.; Yi, Z.; Deng, R.; Liang, L.; Xie, X.; Loong, D. T. B.; Song, S.; Fan, D.; All, A. H.; Zhang, H.; Huang, L.; Liu, X. Binary Temporal Upconversion Codes of Mn^{2+}-Activated Nanoparticles for Multilevel Anti-Counterfeiting. *Nat. Commun.* **2017**, *8* (1), 899.
(27) Liochev, S. I.; Fridovich, I. Carbon Dioxide Mediates Mn(II)-Catalyzed Decomposition of Hydrogen Peroxide and Peroxidation Reactions. *Proc. Natl. Acad. Sci. U.S.A.* **2004**, *101* (34), 12485−12490.

https://doi.org/10.1021/acsanm.4c04307
ACS Appl. Nano Mater. 2024, 7, 21104−21113